

Proton Form Factor Ratio, $\mu_p G_E^p / G_M^p$ from Double Spin Asymmetry

M. Kohl,¹ M. K. Jones,² A. Liyanage,¹ C. Keppel,² E. Christy,¹ S. Choi,³ H-K. Kang,³
Z. E. Meziani,⁴ W. Armstrong,⁴ O. A. Rondon,⁵ D. Crabb,⁵ D. Day,⁵ J. Maxwell,⁵
J. Mulholland,⁵ H. Baghdasaryan,⁵ N. Kalantarians,⁵ L. Ndukum,⁶ and J. Dunne⁶

¹Hampton University, Hampton, Virginia 23668, USA

²Thomas Jefferson National Accelerator Facility, Newport News, Virginia 23606, USA

³Seoul National University, Seoul, Korea

⁴Temple University, Philadelphia, Pennsylvania 19122, USA

⁵University of Virginia, Charlottesville, Virginia 22903, USA

⁶Mississippi State University, Jackson, Mississippi 39262, USA

(Dated: June 21, 2013)

The form factors are fundamental properties of the nucleon representing the effect of its structure on its response to electromagnetic probes such as electrons. The ratio of the electric and magnetic form factors of the proton has been measured for elastic electron-proton scattering up to $Q^2 = 5.66$ (GeV/c)² using the double spin asymmetry for target spin orientation aligned perpendicular to the beam momentum direction.

This alternative measurement of G_E^p / G_M^p has verified and confirmed the dramatic discrepancy at high Q^2 between the Rosenbluth and the recoil-polarization-transfer method with a different measurement technique and systematic uncertainties uncorrelated to those of the recoil-polarization measurements. The measurement of the form factor ratio at $Q^2 = 2.06$ (GeV/c)² has been determined as $\mu_p G_E^p / G_M^p = 0.605 \pm 0.178_{stat} \pm 0.033_{sys}$ which is in agreement with an earlier measurement with the polarized target technique at similar kinematics. The same measurement at $Q^2 = 5.66$ (GeV/c)² has been determined as $\mu_p G_E^p / G_M^p = 0.672 \pm 0.362_{stat}$ which represents the highest Q^2 reach with the double spin asymmetry to date.

I. INTRODUCTION

Detailed knowledge of the nucleon is very important to understand the nucleus. Electron scattering is the best tool to probe deep inside nucleons and nuclei. In the one-photon exchange (Born) approximation, the structure of the nucleon is characterized by the electric and magnetic (Sachs) form factors $G_E(Q^2)$ and $G_M(Q^2)$, which depend only on the four-momentum transfer squared, Q^2 .

The Rosenbluth separation technique has been the first method to separate the proton form factors G_E^p and G_M^p by measuring the elastic electron scattering cross sections at different angles and energies and fixed Q^2 . In addition, the proton G_E^p / G_M^p ratio has been extracted from measurements of recoil polarization components. By taking the ratio of polarization components, which is proportional to G_E^p / G_M^p , many of the systematic errors of the experiment are canceled. Measurement of the beam-target asymmetry using double polarization experiments with polarized target is a third technique to extract G_E^p / G_M^p which has not been conducted as often as Rosenbluth separation or recoil polarization experiments. For elastic scattering of polarized electrons from a polarized target, the beam-target asymmetry,

$$A_p = \frac{-br \sin \theta^* \cos \phi^* - a \cos \theta^*}{r^2 + c} \quad (1)$$

is directly related to the form factor ratio, $r = G_E^p / G_M^p$. The polar and azimuthal angles, θ^* and ϕ^* describe the orientation of the polarization vector relative to q , where the y axis points perpendicular to the scattering plane defined by the electron three-momenta

($\vec{p}_e \times \vec{p}_{e'}$). The quantities a, b, c are kinematic factors given by $a = 2\tau \tan \frac{\theta_e}{2} \sqrt{1 + \tau + (1 + \tau)^2 \tan^2 \frac{\theta_e}{2}}$, $b = 2 \tan \frac{\theta_e}{2} \sqrt{\tau(1 + \tau)}$ and $c = \tau + 2\tau(1 + \tau) \tan^2 \frac{\theta_e}{2}$ with $\tau = Q^2 / |4M^2|$ and where θ_e is the electron scattering angle.

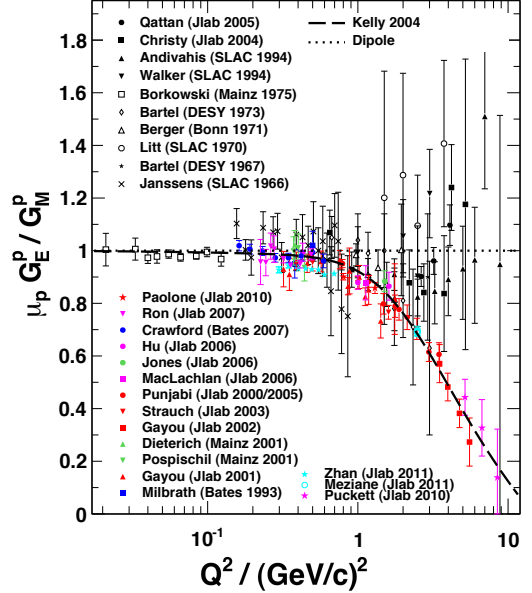


FIG. 1. Proton electric to magnetic form factor ratio from Rosenbluth-separated cross-sections (black symbols) [1–10] and from double-polarization experiments (colored symbols) [11–28]. Theoretical model by Kelly [29] is also shown.

The world data of the proton form factor ratio $\mu_p G_E^p/G_M^p$ ($\mu_p = 2.79$) from the Rosenbluth-separated method [1–10] are shown in Figure 1 along with those obtained from the double polarization experiments with recoil polarization [11–26] and polarized target [27, 28]. A linear fall-off of the polarization data can be seen compared to the nearly flat Q^2 dependence of G_E^p/G_M^p measured with the Rosenbluth technique. One possible solution that explains the difference between the two experimental methods is two-photon exchange (TPE) [30–39].

Having the same sensitivity as the recoil polarization technique to the TPE effects, the third technique, beam-target asymmetry is a good way to verify the systematic errors in the recoil polarization technique. By measuring G_E^p/G_M^p and comparing it to the previous results, the discovery of any unknown or underestimated systematic errors in the previous measurements is possible. The first such measurement was done by the experiment RSS at Jefferson Lab at $Q^2 = 1.5$ (GeV/c)² [28]. Carrying out the same measurement at higher Q^2 values is very important to study the consistency of the third technique, double-spin asymmetry with the first two techniques, Rosenbluth separation and recoil polarization. In this work, the polarized target method is applied at $Q^2 = 2.20, 5.17$, and 6.25 (GeV/c)² as a by-product of the experiment SANE.

Section II presents the description of the experimental setup. Section III presents the detailed description of the data analysis method, including the elastic event selection, raw/physics asymmetry calculation, extraction of the proton form factor ratio, $\mu_p G_E^p/G_M^p$, and estimation of the systematic uncertainties. Section IV presents the final results of the experiment and discuss the impact of the measurement on the world database of proton electromagnetic form factor ratio. An overview of the theoretical uncertainty of the nucleon electromagnetic form factors is also discussed. Section V presents the conclusion.

II. EXPERIMENTAL SETUP

The experiment E07-003 (Spin Asymmetries of the Nucleon Experiment) is a single-arm inclusive-scattering experiment. The goal of SANE was to measure proton spin structure functions $g_1(x, Q^2)$ and $g_2(x, Q^2)$ at four-momentum transfer $2.5 < Q^2 < 6.5$ (GeV/c)² and $0.3 < x < 0.8$ which is an extension of the kinematics of experiment RSS [40] performed in Hall C, Jefferson Lab in 2007.

SANE measured the inclusive spin asymmetries with the target spin aligned parallel and nearly perpendicular (80°) to the beam direction for longitudinally polarized electron scattering from a DNP polarized proton (crystallized NH₃) target. The experiment was carried out in the experimental Hall C at Jefferson Lab from January to March, 2009. A subset of the data was used to measure the elastic beam-target spin asymmetry from elas-

tic electron-proton scattering. Polarized electrons with energies 4.72 GeV and 5.89 GeV were scattered from the polarized proton target with the spin of the proton aligned nearly perpendicular (80°) to the beam direction. Recoiled protons were detected by the High-Momentum Spectrometer (HMS) at 22.3° and 22.0°, and central momenta of 3.58 GeV/c and 4.17 GeV/c, respectively, for the two different beam energies. Scattered electrons were detected by the Big Electron Telescope Array (BETA) in coincidence with the proton in HMS. In addition to that, single-arm electron scattering data were also taken by detecting the elastically scattered electron in the HMS at a central angle of 15.4° and 4.4 GeV/c HMS central momentum for an electron beam energy of 5.89 GeV.

The Continuous Electron Beam Accelerator Facility (CEBAF) at the Thomas Jefferson National Accelerator Facility delivers longitudinally polarized electron beam with ~ 100 % duty factor simultaneously to all three experimental halls. This delivers an 85% polarized electron beam with quantum efficiency of 1%. More information about the CEBAF accelerator can be found in [41].

The fast-raster system with a uniform square beam spot of 1×1 mm² [42, 43], 25 meters upstream of the target is designed to increase the effective beam size in order to prevent damage to the targets due to the high current. The Hall C arc dipole magnets are used as a spectrometer to measure the energy of the electron beam as it enters the Hall. Using the curvature of the beam over its 34.4° deflection by dipoles and the precise knowledge of the arc dipole fields, the energy of the beam is determined with an accuracy of $\Delta E/E \sim 10^{-4}$. The beam polarization was measured by Hall C Møller polarimeter [44].

In addition to the standard Hall C beam-line equipment, SANE required extra beam-line equipment to accommodate the UVa polarized target. The slow-raster was added to spread the beam over an even larger area of the target material cup. This second raster was circular, with a diameter of 2 cm [45]. Because the raster system rapidly changes the actual beam position on the target during the experiment, SANE used the relative position to the beam center by recording the raster X and Y amplitudes in an ADC. When the target magnetic field is nearly perpendicular to the beam, the electron beam is deflected down, away from the target center. To counteract this, the beam was sent through a chicane of magnets which bent it down and then back up at the target so that it does not miss the center of the target. Even after the beam passed through the target center, it would continue to bend down, deflecting away from the standard beam dump in the Hall. Therefore, an 80-foot-long helium bag was used as an additional beam line from the scattering chamber to the beam dump. The exit windows were large enough to accept the different beam deflections 2.8° and 2.2° for the different beam energies 4.72 and 5.89 GeV, respectively.

In order to perform a coincidence experiment with the proton detected in HMS, the electron detector is required

to have a large acceptance to match the electron acceptance to the proton acceptance defined by the HMS collimator. The lead-glass electromagnetic calorimeter, Big-Cal, provides the needed acceptance with enough energy and angular resolution [46]. This has a large solid angle of approximately 0.2 Sr with the face of the calorimeter placed 3.50 m from the target cell [46].

The primary apparatus for the elastic data is based on the superconducting magnetic spectrometer called High Momentum Spectrometer (HMS), which has a large solid angle and momentum acceptance, providing the capability of analyzing high momentum particles (up to 7.4 GeV/c). This equipped with a set of detectors to detect and track charged particles scattered from the target. In the standard configuration, the HMS consists of a pair of gas drift chambers (DC1 and DC2) [47], four planes of scintillator hodoscopes (S1X, S1Y, S2X, S2Y) [48], a gas Cherenkov detector, and a lead-glass calorimeter. The two drift chambers provide the particle tracking information at the focal plane. The scintillator hodoscopes are used for triggering the detector read-out and provide the timing information while the gas Cherenkov detector and the lead-glass calorimeter provide the particle identification.

As a double polarization experiment, SANE requires a polarized nucleon target. Frozen ammonia (NH_3) was utilized as a polarized proton target. In addition to the polarized target, ^{12}C and CH_2 targets were also used for detector calibration purposes. The protons in the NH_3 molecules were polarized using Dynamic Nuclear Polarization (DNP) in a 5 T magnetic field at 1 K temperature [49].

In DNP, nucleons were polarized by transferring the free electron polarization in the medium to the nucleons. These spin transitions, both electron and nucleon spin flips, are forbidden due to the dipole selection rules. Therefore, these transitions are induced by microwave radiation at high magnetic field and low temperature. Because of the strong interaction with the lattice, the electrons reach thermal equilibrium very rapidly (in 10^{-3} S) by relaxation to the lowest energy state, allowing it to flip the spin of another proton. However, due to the weak coupling to the lattice, the relaxation time of the nucleons is much larger, $\sim 10^3$ S. In this way, proton polarizations can be accumulated. The spin direction of the polarized proton can be aligned parallel (positive polarization) or anti-parallel (negative polarization) to the field direction by changing the induced transition frequency applied by microwave radiation. Data were taken at both frequencies. The positive polarization was reached by applying the microwave radiation with a frequency of 140.1 GHz, while the negative polarization was reached by 140.5 GHz. A Nuclear Magnetic Resonance (NMR) system was used to monitor the polarization of the SANE target [50].

Choosing $^{14}\text{NH}_3$ as the polarizable proton target material has several advantages compared to lithium hydride (^7LiH and ^6LiH) which is the other commonly used ir-

radiation doping DNP target material. Its higher maximum achievable polarization ($>90\%$ at 1 K and 5 T), the high rate at which it reaches the maximum polarization (<30 minutes), its higher resistance to radiation damage caused by an experimental beam and the high percentage of polarizable nucleons for scatterings, its dilution factor, which is roughly 17.6% protons for $^{14}\text{NH}_3$, are the crucial properties.

SANE used the University of Virginia polarized target. This replaced the standard Hall C target housing called *scattering chamber*. It consisted of a superconducting Helmholtz pair of magnets which provide a 5 T magnetic field to the target, a target insert, which is roughly 2 m long, provides the room for four target materials, in 2.5 cm diameter target cups, A liquid helium evaporation refrigerator system to keep the target material at 1 K temperature and a NMR system, which provide an online target polarization and recorded the operating conditions.

The microwave horns were trained on each NH_3 target cup to provide the microwave radiation required for target DNP, and the NMR coils were embedded into the two NH_3 target cups to measure the target polarizations. Microwave were provided by the Extended Interaction Oscillator (EIO).

III. DATA ANALYSIS

The determination of the particle trajectory and momentum at the target was done mainly by two major steps. The first step was to find the trajectory, the positions and angles, X_{fp} and X'_{fp} (Y_{fp} and Y'_{fp}) in the dispersive (non-dispersive) direction at the detector focal plane using the two HMS drift chambers. The second step was to reconstruct the trajectory back to the interaction vertex using an HMS optics matrix. Because the optics matrix takes into account the vertical position of the beam at the target, the calculation of momentum and out-of-plane angle are sensitive to the vertical position. The HMS optics matrix has been determined without the target magnetic field. therefore, an additional particle transport through the target magnetic field has been added to the existing HMS particle-tracking algorithm to take account the extra particle deflections due to the target magnetic field.

First, the particle tracks are reconstructed by the HMS reconstruction coefficients to the target center, assuming no target magnetic field. Then, by knowing the target coordinates, the particle is projected back to the field-free region at $z=100$ cm from the target center and then transported back to the target center through the target magnetic field, determining new tracked vertical position. If the difference between this tracked vertical position at the target center and the vertical position of the beam measured by the slow-raster is larger than 1 mm, then a new effective vertical position is assumed and the procedure is iterated until the difference between the tracked

and measured vertical position is less than 1 mm. Standard calibrations for all of the HMS detectors have performed [51].

There are a large number of π^0 events produced in the target. These neutral pions decay very rapidly into two photons. The BigCal calibration was done using the energy deposited in two separated clusters in BigCal from these two neutral photons.

A. Elastic Event Selection

Identification of electrons in HMS is done with the PID and momentum acceptance cuts. By using the Cherenkov cut, number of photoelectrons for the Cherenkov counter >2 and calorimeter cut of $E_{cal}/P > 0.7$, (PID cuts), the background due to π^- particles is suppressed. The quantities, E_{cal} is the deposited energy in the HMS calorimeter. The HMS spectrometer measures the momentum of the detected electron, P .

an acceptance cut on the relative momentum, $\delta = \frac{P-P_c}{P_c} = \frac{\delta P}{P}$, which is well determined for the region of $-8\% < \delta < 10\%$ has been applied to the data in addition to the PID cuts. P_c is the central momentum of HMS. This eliminates events that are outside of the spectrometer acceptance, but end up in the detectors after multiple scattering in the magnets or exit windows. Because the elastic events are mostly populating an higher region of the δ acceptance, $10\% < \delta < 12\%$, where the reconstruction matrix elements are not well known, these data were analyzed separately so that the systematic uncertainty from the HMS optics can be determined separately. Therefore, two δ intervals of the elastic data, $-8\% < \delta < 10\%$ and $10\% < \delta < 12\%$, were used separately in addition to the PID cuts to extract the elastic events. Using this higher δ region of $10\% < \delta < 12\%$ has gained extra events

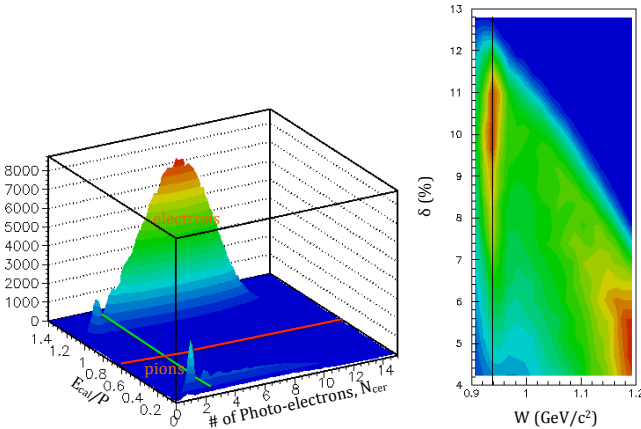


FIG. 2. *Left*: Cherenkov photo electrons and calorimeter energy regions for both pions and electrons. The red (green) line indicate the calorimeter (Cherenkov) cut used to separate electrons. *Right*: The momentum acceptance of the total single-arm electron data as a function of invariant mass.

about $\sim 40\%$.

The extraction of elastic events from the coincidence data has done using both HMS and BigCal quantities. By knowing the electron beam energy, E and measuring the recoil proton angle, θ_p with HMS, the horizontal (vertical) coordinates X (Y) of the scattered electron at the lead-glass calorimeter (BigCal) in BETA were measured (BETA), and also calculated from the elastic kinematics on the proton (HMS). An elliptic cut on $\Delta Y = (Y_{HMS} - Y_{BETA})$ vs $\Delta X = (X_{HMS} - X_{BETA})$,

$$\sqrt{\left(\frac{\Delta X}{X_{cut}}\right)^2 + \left(\frac{\Delta Y}{Y_{cut}}\right)^2} \leq 1.$$

reduces the background most effectively than using the cuts on ΔX and ΔY separately, because the shape of the cut matches the shape of the elastic peak in two dimensional phase space, $(\Delta X, \Delta Y)$. Here, $(X_{cut}, Y_{cut}) = (7, 10)$ cm.

Based on energy and momentum conservation for electron-proton elastic scattering, the relative momentum difference, $\Delta_p = \frac{P - P_p(\theta_p)}{P_c} \times 100$ between the proton momentum measured by HMS, P and the momentum predicted by the scattered proton angle, P_p , using Equation 2,

$$P_p(\theta_p) = \frac{2M_p E(E + M_p) \cos \theta_p}{M_p^2 + 2M_p E + E^2 \sin^2 \theta_p}, \quad (2)$$

which is expressed as a percentage of the HMS central momentum, P_c is defined. The width of the Δ_p cut was chosen to be $\pm 3\sigma \simeq \pm 0.02$ and applied for further background suppression for the coincidence data.

The beam and target offsets were determined on data using data-to-Monte Carlo simulation comparison for both single-arm and coincidence data. In single-arm data, the invariant mass, W had a slight dependence on the out-of-plane angle at the target. In addition, in coincidence data, Δ_p (Y_{BETA}) had a dependence on the out-of-plane angle at the target (ΔY). An azimuthal angle dependence was added to the target field map used in the calculation of the electron track that changed the

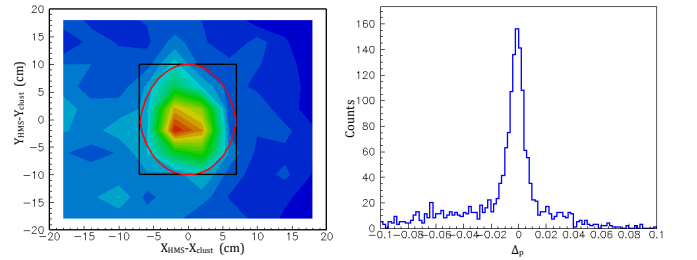


FIG. 3. *Left*: Elliptical cut (red) with $(X_{cut}, Y_{cut}) = (7, 10)$ cm applied to the ΔY vs ΔX spectra at $Q^2 = 6.26$ (GeV/c²). *Right*: Δ_p spectra of all events after applying the elliptical cut at $Q^2 = 6.26$ (GeV/c²).

electron's reconstructed momentum and hence the reconstructed vertical position, which eliminated the above dependencies.

B. Raw/ Physics Asymmetries

The measured asymmetry on the extracted elastic events is formed by,

$$A_r = \frac{N^+ - N^-}{N^+ + N^-} \quad (3)$$

where, N^+ and N^- are the raw elastic counts normalized by the deadtime-corrected charge for opposite beam helicities. Hence the physics asymmetry,

$$A_p = \frac{A_r}{P_B P_T f} + N_c \quad (4)$$

is obtained by normalizing the measured asymmetry, A_r by target and beam polarizations, P_T and P_B , and the dilution factor, f . The dilution factor is the ratio of the yields from scattering off free protons to that from the entire target. It is only involves materials in the beam, off which electrons can scatter. The N_c term is a correction to the measured asymmetry that eliminates the contribution from quasi-elastic scattering off polarized ^{15}N under the elastic peak. Because SANE used $^{14}\text{NH}_3$ (ammonia), the correction by N_c for ^{14}N is negligible but of opposite sign as for ^{15}N [28].

A Monte Carlo simulation was used to estimate the backgrounds and to determine the dilution factor, f . The target ladder was immersed in a liquid He bath to maintain temperature 1 K, cooled down from 4 K by the pumping of the liquid with the evaporation refrigerator in order to optimize the target polarization. Therefore, for NH_3 in the liquid He bath, H , N , He and Al were simulated and compared with the single-arm elastic data. The material Al Contributions arise from the target cup lids, the 4 K shield and the refrigerator's tailpiece. Because two different NH_3 target cups have been used with different packing fractions, the dilution factors were determined separately. The packing fraction is the ratio of the volume taken by the ammonia to the target cup volume which is determined by comparing measured and simulated yields.

The dilution factors were calculated for both targets by taking the ratio of the difference between the total raw yields and the Monte Carlo background yields ($N + \text{He} + \text{Al}$) to the total raw yield.

$$f = \frac{\text{Yield}_{\text{data}} - \text{MC}_{(N+\text{He}+\text{Al})}}{\text{Yield}_{\text{data}}}. \quad (5)$$

The obtained dilution factors are shown in Figure 4 (right) for top target for two different δ regions.

The physics asymmetry, A_p and its error, ΔA_p were calculated for the extracted elastic events using Equation 4 by using average values for $P_B = 73\%$, $P_T = 70\%$,

and normalizing with the dilution factor, f for each W bin. The constant physics asymmetries and their errors were determined for both top and bottom targets by using a linear fit in the region of $0.91 < W < 0.97 \text{ GeV}/c^2$, where A_p is constant. Figure 5 (left) shows the top and bottom physics asymmetries for the two different δ regions. The weighted average A_p and ΔA_p were obtained by combining the top and bottom asymmetries for both δ regions. The results are shown in Figure 5 (right).

The background shape under the elastic peak for the coincidence data was generated using the carbon target. The simulated carbon background was then normalized by scaling factor determined, using the ratio of data-to-SIMC yields for the region of $0.03 < \delta p/p < 0.08$ where the data and the simulated carbon background match each other. By adding this normalized carbon background to the SIMC-simulated H , a better match between the total data and SIMC-simulated $\text{H} + \text{C}$ can be seen in Figure 6 (left). Because the coincidence data were taken for two beam energies of 5.89 GeV and 4.73 GeV, this background simulation is done separately for both energies. The dilution factor is then calculated using Equation 5. Here, for Equation 5, carbon was used instead of $\text{N} + \text{He} + \text{Al}$. Because of the low statistics, the average dilution factor was calculated using the integrals of both the normalized carbon MC and the measured counts under the elastic peak over the $\delta p/p$ region with a narrower cut of ± 0.02 instead of normalizing the raw asymmetry bin-by-bin with the dilution factor, f as a function of $\delta p/p$. The dilution factors calculated from the integration method for the top and bottom targets for the 5.895 GeV beam energy is determined as 0.785 and 0.830, respectively, while that for the 4.73 GeV beam energy is determined as 0.816.

To have better statistics from the low statistics coincidence data, all the coincidence runs were separated to a few categories at first, the data taken from top and bottom targets, positive and negative beam and target polarizations for each target cup, and so on. By normalizing $A_r/P_B/P_T$ with the calculated dilution factors, the physics asymmetries, A_p were obtained for each category of data. Figure 6 (right) shows the extracted physics asymmetries for different categories for both beam energies.

The weighted average physics asymmetries and their errors were calculated for the two beam energies as $A = 0.006 \pm 0.077$ for the beam energy of 5.893 GeV, and $A = 0.184 \pm 0.136$ for the beam energy of 4.725 GeV. These results are also shown in the same Figure 6 (right)

C. Extraction of G_E^p/G_M^p Ratio

The beam-target asymmetry, A_p for elastic electron-proton scattering is directly related to the proton elastic form factor ratio, G_E^p/G_M^p as in Equation 1. Therefore, using Equation 1, G_E^p/G_M^p can be determined directly from A_p using the formula:

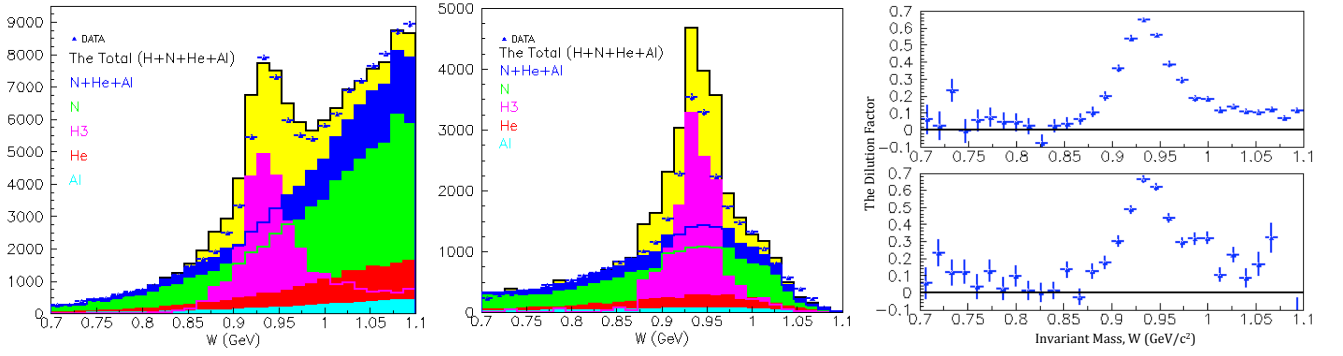


FIG. 4. The simulated target contributions at the elastic peak compared to the data at both δ regions, $-8\% < \delta < 10\%$ (left) and $10\% < \delta < 12\%$ (center) for the top target using experiment run 72795. Different colors show different target type contributions. Right: The calculated dilution factor for $-8\% < \delta < 10\%$ (top) and $10\% < \delta < 12\%$ (bottom) for the top target using run 72795.

$$\frac{G_E^p}{G_M^p} = -\frac{b}{2A_p} \sin \theta^* \cos \phi^* \quad (6)$$

$$+ \sqrt{\frac{b^2}{4A_p^2} \sin^2 \theta^* \cos^2 \phi^* - \frac{a}{A_p} \cos \theta^* - c}$$

The four-momentum transfer squared, $Q^2(E, E', \theta_e)$ for the elastic events were extracted by comparing with the Monte Carlo simulation yields. After applying all of the elastic event selection cuts on both data and MC yields, the simulated background yields were subtracted from the data and the mean values of Q^2 read from the resulting Q^2 distribution. The mean of the measured (calculated using elastic kinematics of the proton in HMS) electron scattering angle, θ_e was determined by applying all of the electron selection cuts on single-arm (coincidence) data. The polar and azimuthal angles, θ^* and ϕ^* are calculated as,

$$\theta^* = \arccos(-\sin \theta_q \cos \phi_e \sin \beta + \cos \theta_q \cos \beta) \quad (7)$$

$$\phi^* = -\arctan\left(\frac{\sin \phi_e \sin \beta}{\cos \theta_q \cos \phi_e \sin \beta + \sin \theta_q \cos \beta}\right) + 180^\circ.$$

The out-of-plane angle of the scattered electron, ϕ_e is estimated by reading the mean value of the measured ϕ_e distribution for the elastic events. The three-momentum transfer vector, \vec{q} points at an angle of θ_q , which is the scattered proton angle determined (measured) event-by-event by the elastic kinematics of the electron (proton) in HMS, and the mean value of θ_q was determined using the θ_q distribution. The angle β is the target magnetic field direction, 80° to the beam Z axis toward the BETA detector package.

Equation 6 has two solutions for G_E^p/G_M^p . The positive value was chosen because the negative value is non physical. The errors of the form factor ratio G_E^p/G_M^p , Δr were determined by propagating the errors of the physics

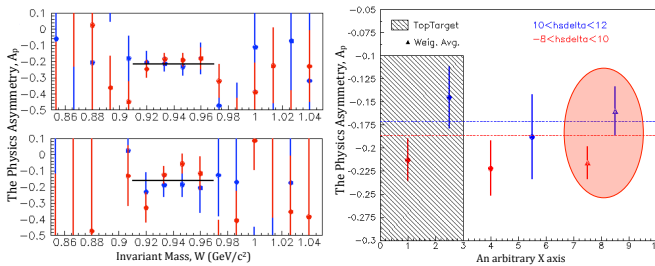


FIG. 5. (Left): The top and bottom target physics asymmetries for the two different δ regions $-8\% < \delta < 10\%$ (top) and $10\% < \delta < 12\%$ (bottom). (Right): The constant physics asymmetries for both top (inside the hatched box) and bottom (outside the hatched box) targets and the weighted average of it (inside the ellipse) for two different δ regions. The expected physics asymmetries from the known form factor ratio for each Q^2 by Kelly's form factor parametrization [29] are also shown by dashed lines separately for the two different δ regions.

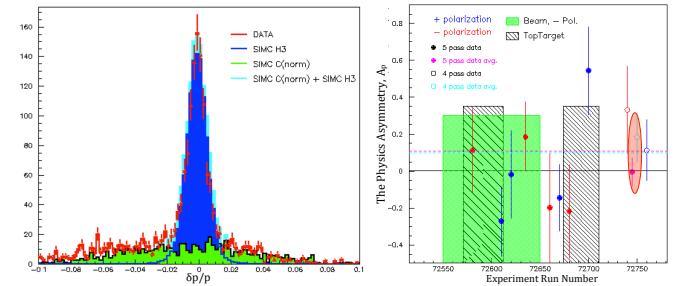


FIG. 6. Left: The normalized carbon background and H comparison with the coincidence data for the beam energy 5.89 GeV. Right: The physics asymmetries for each category of the coincidence data. The solid circles show the data from 5.895 GeV beam energy while the empty circles show those at 4.73 GeV beam energy. The X axis shows the run numbers. The weighted average physics asymmetries and their errors for the two beam energies are also shown (inside the brown ellipse). The dashed lines are at the expected values of the physics asymmetries for the two beam energies 4.73 GeV (light blue) and 5.893 GeV (magenta) calculated from the known form factor ratio for each Q^2 by Kelly's form factor parametrization [29].

asymmetry, ΔA_p .

The physics asymmetries A_p , and extracted proton form factor ratios, $r = G_E^p/G_M^p$ together with the experimental parameters for both single-arm and coincidence data are shown in Table I.

D. Systematic Error Estimation

The errors arising from the kinematic quantities were estimated by varying each quantity (one at a time) by its corresponding uncertainty (0.05% for the beam energy, 0.1% for the central momenta, and 0.5 mrad for the spectrometer angle) and propagating it to the Monte Carlo extracted G_E^p/G_M^p ratio. The resulting difference in the extracted G_E^p/G_M^p ratio from the value at the nominal kinematics is taken as the uncertainty in the G_E^p/G_M^p ratio due to the uncertainty in that quantity. In general, the uncertainties due to the kinematic variables are less than 1%.

Using the Jacobian of the elastic electron-proton reaction, the error on the θ_q , $\delta\theta_q$ propagated from the beam energy E and the scattered electron angle θ_e was determined as 0.03° . In addition, using the uncertainty on the target magnetic field direction, β , $\delta\beta = 0.1^\circ$, the uncertainties on the θ^* and ϕ^* were determined. Hence, the error on the G_E^p/G_M^p from the error on the θ^* was determined as 0.54%, while that from the ϕ^* was determined as 0.01%.

The accuracy of the target polarization is based on the accuracy of the calibration constants used to produce the polarization from the NMR area. The systematic error on the target polarization was estimated as 5% [50]. The error on the beam polarization measurement comes from a global error of the Möller measurements and the error due to the fit to these measurements. The beam polarization uncertainty during SANE is measured as 1.5% [50].

For both single-arm and coincidence data sets, the dilution factor has been determined using data-to-Monte Carlo simulated yields comparisons. Therefore, the uncertainty of the dilution factor is based on how well the data match with the simulated yield. Since the simulated yields are based on the packing fraction, the error of 5% in the packing fraction measurement propagates to the dilution factor and hence the uncertainty on the form factor ratio, G_E^p/G_M^p is determined as 1.34%.

Single-arm data used the extended momentum acceptance in the region of $10\% < \delta < 12\%$, where the HMS optics are not well tested. Therefore, the reconstruction of the events from this region is not understood well and the uncertainty in the COSY model used to determine these particle tracks is a special source of systematic uncertainty for the single-arm data. This has been tested with a Monte Carlo simulation. The biggest loss of events in this higher δ region, $10\% < \delta < 12\%$ is identified as at the HMS vacuum pipe exit. The uncertainty due to this higher momentum electron tracks hitting the edge of the

vacuum pipe exit was determined by applying ± 2 mm offsets on the vacuum pipe positions on both vertical and horizontal directions separately, and taking the effective solid angle differences between the offsets and those at the nominal vacuum pipe position. Taking the average ratio of these effective solid-angle differences to the nominal solid-angle, the uncertainty due to the particle track reconstruction has been estimated as 0.68%. However, during the dilution factor determination, Monte Carlo simulated C cross-section shape match was done for data in both δ regions. Also, Monte Carlo yields were normalized with the ratio of data-to-Monte Carlo yields in the region $0.7 < W < 0.85$ GeV/c². Therefore, the uncertainty, 0.68% that comes from losing events due to higher δ are already accounted in the dilution factors.

Table II summarizes non-negligible contributions to the systematic uncertainty of the single-arm data. The measurements, the uncertainty of each measurement and the relative systematic uncertainty of the $\mu_p G_E^p/G_M^p$ ratio ($=\mu_p r$) due to the uncertainty on that measurement are shown. The final relative systematic uncertainty was obtained by summing all the individual contributions quadratically. Summing all the individual contributions of the systematic uncertainties linearly represents the maximum possible error of the measurement. Therefore, the final relative systematic error on $\mu_p G_E^p/G_M^p$ was estimated as 5.44% while the maximum possible error was estimated as 9.13%. The target, beam polarizations and the packing fraction are the dominant contributions to the systematic uncertainty.

IV. RESULTS AND DISCUSSION

The results for the proton elastic form factor ratio, $\mu_p G_E^p/G_M^p$ determined from both data sets, single-arm and coincidence, are shown in Table I. The resulting form factor ratio from the two regions of the HMS momentum acceptance was determined by extrapolating both measurements to the average Q^2 using the parametrization by Kelly [29], as in Equation 8 and then taking the weighted average, resulting in $\mu_p G_E^p/G_M^p = 0.605 \pm 0.178$ (only the statistical error is shown) for an average four-momentum transfer squared $Q^2 = 2.06$ (GeV/c)².

$$(\mu_p r)_{ext} = (\mu_p r)_{exp} + \left(\frac{\Delta(\mu_p r)}{\Delta Q^2} \right) \cdot (\langle Q^2 \rangle - Q_{exp}^2). \quad (8)$$

Where the quantities $(\mu_p r)_{ext}$ is the extrapolated form factor ratio using the parameterization by Kelly [29], $(\mu_p r)_{exp}$ is the form factor ratio from the experiment, $\left(\frac{\Delta(\mu_p r)}{\Delta Q^2} \right)$ is the straight-line gradient to Kelly's parameterization [29], $\langle Q^2 \rangle$ is the average Q^2 , and Q_{exp}^2 is the experiment Q^2 from data.

Due to the low statistics of the coincidence data, the statistical errors of the $\mu_p G_E^p/G_M^p$ ratios are larger at both beam energies, corresponding to $Q^2=5.17$ and 6.26

	single-arm		Coincidence	
	$-8\% < \delta < 10\%$	$10\% < \delta < 12\%$		
E (GeV)	5.895	5.895	5.893	4.725
θ_q (Deg)	44.38	46.50	22.23	22.60
ϕ_q (Deg)	171.80	172.20	188.40	190.90
θ_e (Deg)	15.45	14.92	37.08	43.52
ϕ_e (Deg)	351.80	352.10	8.40	10.95
Q^2 (GeV/c) ²	2.20	1.91	6.19	5.14
θ^* (Deg)	36.31	34.20	101.90	102.10
ϕ^* (Deg)	193.72	193.94	8.40	11.01
$A_p \pm \Delta A_p$	-0.216 ± 0.018	-0.160 ± 0.027	-0.006 ± 0.077	0.184 ± 0.136
$\mu_p r \pm \Delta(\mu_p r)$	0.483 ± 0.211	0.872 ± 0.329	0.937 ± 0.428	-0.052 ± 0.678
predicted $\mu_p r$	0.73	0.78	0.305	0.38
predicted A_p	-0.186	-0.171	0.107	0.097

TABLE I. The physics asymmetries, A_p and extracted form factor ratios, $\mu_p r$ together with the experimental parameters for both single-arm and coincidence data. The expected ratio $\mu_p r$ from Kelly's form factor parametrization [29] for each Q^2 and the calculated A_p from the above predicted $\mu_p r$ are also shown. The errors ΔA_p and $\Delta(\mu_p r)$ are statistical.

Measurement	Error	$\Delta(\mu_p r)/\mu_p r$ (%)
E (GeV)	0.003	0.07
E' (GeV)	0.004	0.13
θ_e (mrad)	0.5	0.54
θ^* (mrad)	1.22	0.54
ϕ^* (mrad)	0.3	0.01
P_T (%)	5.0	5.0
P_B (%)	1.5	1.5
Packing Fraction, pf (%)	5	1.34
The maximum possible error		9.13
The final error		5.44

TABLE II. Systematic uncertainty on each measurement and the relative systematic uncertainty on the $\mu_p G_E^p/G_M^p$ ratio due to the uncertainty on that measurement for the single-arm data. The maximum possible systematic uncertainty obtained by summing all the individual contributions linearly and the final systematic uncertainty obtained by summing all the individual contributions quadratically are also shown.

(GeV/c)². Therefore, the weighted average $\mu_p G_E^p/G_M^p$ and its error were also determined from the measurements extrapolated to the average Q^2 using the parametrization by Kelly [29] as in Equation 8 for the two energy settings. The resulting form factor ratio is given as $\mu_p G_E^p/G_M^p = 0.672 \pm 0.362$ (only the statistical error is shown) for an average $Q^2 = 5.66$ (GeV/c)².

Table III shows the final $\mu_p G_E^p/G_M^p$ ratios with the statistical and systematic uncertainties together with the average Q^2 values. Because the form factor ratio at higher Q^2 of 5.66 (GeV/c)² is largely dominated by the statistical uncertainty, the systematic uncertainty for this measurement was not studied.

Figure 7 shows the form factor measurements from SANE together with the world data as a function of Q^2 . The inner-error bar shown at $Q^2 = 2.06$ (GeV/c)² is statistical and the outer-error bar is a combination of statistical and systematics. The error bar shown at $Q^2 = 5.66$ (GeV/c)² is only statistical. The weighted average data point at $Q^2 = 2.06$ (GeV/c)² is very consis-

Q_{Avg}^2 (GeV/c) ²	$\mu_p r \pm \Delta\mu_p r_{(stat)} \pm \Delta\mu_p r_{(syst)}$
2.06	$0.605 \pm 0.178 \pm 0.033$
5.66	0.672 ± 0.362

TABLE III. The results of the form factor analysis from the experiment SANE. Both the statistical and systematic uncertainties are shown for the lower $Q^2 = 2.06$ (GeV/c)² while only the statistical uncertainty is shown for the higher $Q^2 = 5.66$ (GeV/c)².

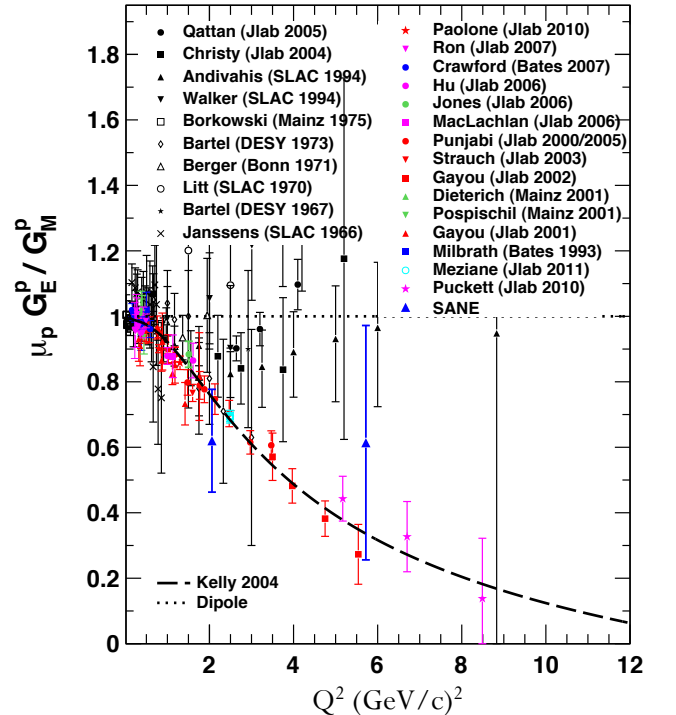


FIG. 7. The form factor measurements from SANE together with the world data as a function of Q^2 . The inner-error bar shown at $Q^2 = 2.06$ (GeV/c)² is statistical and the outer-error bar is a combination of statistical and systematics. The error bar shown at $Q^2 = 5.66$ (GeV/c)² is only statistical.

tent with the existing recoil-polarization measurements, confirming the decrease of $\mu_p G_E^p/G_M^p$ with Q^2 . Because in theory, the beam-target asymmetry method is equivalent to the polarization-transfer method, the results are expected to be similar to the polarization-transfer data. The measurement does not reveal any unknown systematic difference from the polarization-transfer method. The obtained accuracy confirms the suitability of using the beam-target asymmetry for determination of the $\mu_p G_E^p/G_M^p$ ratio.

The weighted average data point at higher $Q^2 = 5.66$ (GeV/c)² has a larger statistical uncertainty due to the small number of counts which makes it difficult to draw a strong conclusion with respect to a change of the proton form factor ratio with Q^2 .

The HMS drift chamber gas leak during the coincidence data taking resulted about ~ 60 % inefficiency of the elastic proton detection by HMS. In addition, due to a damage of the superconducting Helmholtz coils used to polarize the NH₃ target, the production data-taking time was reduced. Therefore, single-arm data were taken only about ~ 12 hours in total and the coincidence data for elastic kinematics were taken about a week for both beam energies, ~ 14 hours and ~ 155 hours, respectively, for two beam energies 4.72 GeV and 5.89 GeV. Therefore, along with optimum proton detection efficiency in HMS, it should be possible to take at least four times the amount of data in the same time period, which would decrease the error bars on both measurements by a factor of two. In addition, the target spin orientation was not optimized for a measurement of G_E/G_M .

V. THEORETICAL INTERPRETATION

The experimental understanding of the proton form factors led to many theoretical attempts to explain the nucleon form factors. Despite their approximations and limitations, some of these non-perturbative methods reveal some insight into the nucleon structure.

In non-relativistic approximation, G_E and G_M are the Fourier transforms of the charge and magnetic moment densities of the nucleon in the Breit frame. However, only at $Q^2 = 0$, the Breit frame coincides with the lab frame and the form factor interpretation to the charge and magnetic moment distribution become valid. Kelly [29] has derived a theoretical model relating the Sachs form factors to the rest frame charge and magnetic moment densities taking relativity into account. However, this is strictly model-dependent since the Lorentz boost for a composite object such as proton depends on the interactions among the constituent quarks. The most important feature of the proton density from this model is the broader shape of the charge density relative to the magnetic moment density, reflecting the precise recoil-polarization data in which G_E^p falls faster than G_M^p at large Q^2 .

The earliest model, Vector Meson Dominance (VMD)

explained the dipole behavior of the nucleon form factors. In this model, the photon couples to the nucleon through the exchange of the three lightest vector mesons, ρ (770), ω (782) and ϕ (1020). In elastic electron-nucleon scattering, the form factors at low Q^2 are dominated by these vector mesons. The first VMD fit was performed by Iachello *et al.* [52] and a linear decrease of the proton $\mu_p G_E^p/G_M^p$ ratio has been predicted for $Q^2 > 1$ (GeV/c)², which is an agreement with the result from the polarization-transfer technique. Gari and Krumpelmann [53] extended the model to conform with pQCD scaling at larger Q^2 with a smooth transition from VMD picture hold at low Q^2 . Thereafter, many extended VMD fits have been obtained which provided a good parameterization of nucleon electromagnetic form factors [54–57].

Constituent Quark Models (CQM) were developed to understand the structure of the nucleons in terms of quark and gluon degrees of freedom. The Isgur-Karl model [58] is an example, in which the quarks are confined by a long-range harmonic oscillator potential supplemented by a short-range one-gluon-exchange quark-quark interaction. Since the quarks are much lighter than the nucleon; they need to be treated relativistically following the prescriptions by Dirac [59], which describes the form factor behavior at large Q^2 . However, a pion cloud and a finite size of the constituent quarks were introduced to this model to correctly describe the behavior at lower Q^2 . Miller [60] added the effects of the pion cloud of the nucleon to the relativistic constituent quark model (rCQM) of the Light-Front Cloudy Bag Model [61] which involves relativistic pion-nucleon form factors. The pion cloud effects within this model made large contributions at low Q^2 , particularly for the neutron electric form factor, which is not well reproduced by the rCQM alone. In contrast, quarks are found to dominate at large Q^2 .

At higher Q^2 , quarks and gluons play a dominant role in the form factors in which the perturbative QCD (pQCD) makes a prediction about the behavior of these. The constancy of the Rosenbluth data for $\mu_p G_E^p/G_M^p$ was consisted with the pQCD dimensional scaling laws [62], valid for asymptotically large Q^2 . These predictions are different from the polarization-transfer measurements, where the ratio $R = \mu_p G_E^p/G_M^p$ shows roughly a linear decrease with Q^2 and points toward a zero-crossing at some larger Q^2 . The decrease of R with Q^2 was later interpreted in pQCD by Belitsky *et al.* [63] introducing the quark orbital angular momentum. The recoil-polarization data for F_2^p/F_1^p are compatible with such a scaling for the entire Q^2 range of the data.

Generalized Parton Distributions (GPDs) are the theoretical framework to understand the quark structure of the nucleon. The predictions for the nucleon form factors are derived using a model for the GPDs by Guidal *et al.* [64], which achieves a very good agreement with experimental data for all four nucleon form factors in the entire Q^2 range. Because GPDs can be related to the total angular momentum carried by the quark in the nucleon, it allows an evaluation of Ji's angular momentum

sum rules [65]. Furthermore, the vector GPDs have been used to derive model-independent representations of the nucleon transverse charge and magnetization densities as two-dimensional Fourier transforms of the Dirac (F_1) and Pauli (F_2) form factors [66].

a complementary framework for studying the form factors is via Dyson-Schwinger Equations (DSEs) [67, 68]. The investigation of hadron structure in the Dyson-Schwinger approach proceeds for baryons via the covariant Faddeev Equation [69, 70]. This approach provides access to all momentum scales and all quark masses, which is in good agreement in form factor results with the experimental data above $Q^2 \simeq 2$ (GeV/c)². This has been shown that the orbital angular momentum contributes one-third to the nucleon spin, and this contribution slowly decrease with rising current quark mass.

Quark-diquark model studies also found a zero-crossing, where its location depends on the model parameters in the calculation [71, 72]. The overall agreement between the [70] and those obtained in the quark-diquark model provides further evidence for the quark-diquark structure of the nucleon.

Lattice gauge theory can provide an *ab initio* calculation in contrast to the all of the other models which have constructed to focuss on selected aspects of QCD. One of the most advanced lattice calculations of electromagnetic form factors has been performed by the QCDSF collaboration [73]. Ashley *et al.* [74] have extrapolated the results of these calculations appropriate to full QCD. Lattice QCD results from LHPC Collaboration [75] performed for the nucleon electromagnetic form factors shows that the Dirac isovector form factor F_1^V in qualitative agreement with data and the isovector ratio F_2^V/F_1^V approaches the experimental results when decreasing m_ϕ from 360 MeV. An extensive discussion

of the theoretical model explanation on the form factors can be found in the review paper [76].

VI. CONCLUSION

Measurement of the beam-target asymmetry in elastic electron-proton scattering offers an independent technique of determining the proton elastic form factor ratio, $\mu_p G_E^p/G_M^p$. The TPE amplitude has a strong ϵ dependence with a large effect on the extraction of the proton form factors from the Rosenbluth separation method. The absence of such a strong dependence for the polarizable observables, the double-spin polarization experiments show a strong validation of the method of measuring the form factor ratio.

The form factor analysis from the experiment SANE extended the proton electric-to-magnetic form factor ratio, $\mu_p G_E^p/G_M^p$ from the double-spin asymmetry up to $Q^2 = 5.66$ (GeV/c)². The results at $Q^2 = 2.06$ (GeV/c)² are an important test of the reproducibility of the first measurement of the beam-target asymmetry at $Q^2 = 1.5$ (GeV/c)² [28]. A measurement with this method at higher Q^2 than the first measurement at $Q^2 = 1.5$ (GeV/c)² has been very important to see if this third technique is consistent with the polarization-transfer method as expected, or if it follows the form factor scaling result from the Rosenbluth separation method. The result of this work validates those of the polarization-transfer method and, therefore, strengthens the case for the TPE framework as an explanation for the form factor discrepancy between unpolarized and polarized data.

However, as a byproduct measurement of the SANE experiment, the precision of this result is limited by statistics. It would certainly be possible to improve the precision at high Q^2 with a dedicated experiment.

-
- [1] I. A. Q. *et al.*, Phys. Rev. Lett., **94**, 142301 (2005).
 - [2] M. E. Christy *et al.*, Phys. Rev. C, **70**, 015206 (2004).
 - [3] L. A. *et al.*, Phys. Rev. Lett., **D 50**, 5491 (1994).
 - [4] R. C. W. *et al.*, Phys. Rev. Lett., **D 49**, 5671 (1994).
 - [5] F. B. *et al.*, Nucl. Phys., **B 93**, 461 (1975).
 - [6] F. B. *et al.*, Nucl. Phys., **A 222**, 269 (1974).
 - [7] W. B. *et al.*, Nucl. Phys., **B 58**, 429 (1973).
 - [8] C. B. *et al.*, Phys. Lett., **B 35**, 87 (1971).
 - [9] J. L. *et al.*, Phys. Lett., **B 31**, 40 (1970).
 - [10] T. J. *et al.*, Phys. Rev., **142**, 922 (1966).
 - [11] M. M. *et al.* (GEP2 γ Collaboration), Phys.Rev.Lett., **106**, 132501 (2011), arXiv:1012.0339 [nucl-ex].
 - [12] A. J. R. P. *et al.*, Phys. Rev. Lett., **104**, 242301 (2010).
 - [13] M. P. *et al.*, Phys.Rev.Lett., **105**, 072001 (2010), arXiv:1002.2188 [nucl-ex].
 - [14] G. R. *et al.*, Phys.Rev.Lett., **99**, 202002 (2007), arXiv:0706.0128 [nucl-ex].
 - [15] Hu, B., and M. K. J. *et al.*, Phys.Rev., **C73**, 064004 (2006), arXiv:nucl-ex/0601025 [nucl-ex].
 - [16] G. M. *et al.*, Nucl.Phys., **A764**, 261 (2006).
 - [17] V. Punjabi and C. F. P. *et al.* (Jefferson Lab Hall A Collaboration), Phys. Rev. C, **71**, 069902 (2005).
 - [18] V. Punjabi and P. *et al.* (Jefferson Lab Hall A Collaboration), Phys. Rev. C, **71**, 055202,Erratum (2005).
 - [19] S. S. *et al.* (Jefferson Lab E93-049), Phys.Rev.Lett., **91**, 052301 (2003), arXiv:nucl-ex/0211022 [nucl-ex].
 - [20] O. Gayou *et al.* (Jefferson Lab Hall A Collaboration), Phys.Rev.Lett., **88**, 092301 (2002), arXiv:nucl-ex/0111010 [nucl-ex].
 - [21] O. G. *et al.*, Phys.Rev., **C64**, 038202 (2001).
 - [22] S. D. *et al.*, Phys.Lett., **B500**, 47 (2001), arXiv:nucl-ex/0011008 [nucl-ex].
 - [23] T. P. *et al.* (A1 Collaboration), Eur.Phys.J., **A12**, 125 (2001).
 - [24] M. K. J. *et al.* (Jefferson Lab Hall A Collaboration), Phys.Rev.Lett., **84**, 1398 (2000 (superseded by [17, 18]), arXiv:nucl-ex/9910005 [nucl-ex].
 - [25] B. D. M. *et al.* (Bates FPP collaboration), Erratum-ibid, **82**, 2221 (1999), arXiv:nucl-ex/9712006 [nucl-ex].
 - [26] B. D. M. *et al.* (Bates FPP collaboration),

- Phys.Rev.Lett., **80**, 452 (1998), arXiv:nucl-ex/9712006 [nucl-ex].
- [27] C. B. C. *et al.*, Phys. Rev. Lett., **98**, 052301 (2007).
- [28] M. K. J. *et al.* (Resonance Spin Structure Collaboration), Phys. Rev. C, **74**, 035201 (2006).
- [29] J. J. Kelly, Phys.Rev., **C70**, 068202 (2004).
- [30] N. Kivel and M. Vanderhaeghen, Phys.Rev.Lett., **103**, 092004 (2009), arXiv:0905.0282 [hep-ph].
- [31] D. Borisyuk and A. Kobushkin, Phys.Rev., **D79**, 034001 (2009), arXiv:0811.0266 [hep-ph].
- [32] D. Borisyuk and A. Kobushkin, Phys.Rev., **C78**, 025208 (2008), arXiv:0804.4128 [nucl-th].
- [33] D. Borisyuk and A. Kobushkin, Phys.Rev., **C74**, 065203 (2006), arXiv:nucl-th/0606030 [nucl-th].
- [34] Blunden, P.G., Melnitchouk, W., Tjon, and J.A., Phys.Rev., **C72**, 034612 (2005), arXiv:nucl-th/0506039 [nucl-th].
- [35] A. V. Afanasev, S. J. Brodsky, C. E. Carlson, Y.-C. Chen, and M. Vanderhaeghen, Phys.Rev., **D72**, 013008 (2005), arXiv:hep-ph/0502013 [hep-ph].
- [36] Y. C. Chen, A. Afanasev, S. J. Brodsky, C. E. Carlson, and M. Vanderhaeghen, Phys.Rev.Lett., **93**, 122301 (2004), arXiv:hep-ph/0403058 [hep-ph].
- [37] M. P. Rekalo and E. Tomasi-Gustafsson, Eur.Phys.J., **A22**, 331 (2004), arXiv:nucl-th/0307066 [nucl-th].
- [38] P. A. M. Guichon and M. Vanderhaeghen, Phys.Rev.Lett., **91**, 142303 (2003), arXiv:hep-ph/0306007 [hep-ph].
- [39] P. G. Blunden, W. Melnitchouk, and J. A. Tjon, Phys.Rev.Lett., **91**, 142304 (2003), arXiv:nucl-th/0306076 [nucl-th].
- [40] F. R. W. *et al.* (RSS Collaboration), Phys. Rev. Lett. **98**, 132003 (2007) ().
- [41] C. W. Leemann, D. R. Douglas, and G. A. Krafft, Ann. Rev. Nucl. Part. Sci. **51**, 413-450 (2001).
- [42] C. Y. *et al.*, Nucl. Instrum. Meth. A **365**, 46-48 (1995) ().
- [43] C. Yan, N. Sinkine, and R. Wojcik, Nucl. Instrum. Meth. A **539**, 1-15 (2005).
- [44] M. H. *et al.*, Nucl. Instrum. Meth. A **462**, 382-392 (2001) ().
- [45] M. Fukuda, S. Okumura, and K. Arakawa, Nucl. Instrum. Meth. A **396**, 45-49 (1997).
- [46] A. J. R. Puckett, **Ph.D. theses, Massachusetts Institute of Technology, (2010)**.
- [47] O. K. B. *et al.*, Nucl. Instrum. Meth. A **367**, 92-95 (1995) ().
- [48] J. Arrington, **Ph.D. theses, California Institute of Technology, (1998)**.
- [49] T. D. A. *et al.*, Nucl.Instrum.Meth., **A427**, 440 (1999).
- [50] J. D. Maxwell, **Ph.D. theses, University of Virginia, (2011)**.
- [51] https://hallcweb.jlab.org/document/howtos/tof_calibration.
- [52] F. Iachello, A. Jackson, and A. Lande, Phys. Lett. B **43**, 191-196 (1973).
- [53] M. Gari and W. Krumpelmann, Z. Phys. A **322**, 689-693 (1985).
- [54] M. A. Belushkin, H. W. Hammer, and U. G. Meissner, Phys. Rev. C **75**, 035202 (2007).
- [55] I. T. L. *et al.*, Eur. Phys. J. A **48**, 151 (2012) ().
- [56] C. C. *et al.*, Phys. Rev. C **82**, 045211 (2010) ().
- [57] E. L. Lomon and S. Pacetti, Phys. Rev. D **85**, 113004 (2012).
- [58] N. Isgur and G. Karl, Phys. Rev. D **18**, 4187 (1978).
- [59] Dirac and A. M. Paul, Rev. Mod. Phys. **21**, 392-399 (1949).
- [60] G. A. Miller, Phys. Rev. C **66**, 032201 (2002) ().
- [61] M. R. Frank, B. K. Jennings, and G. A. Miller, Phys. Rev. C **54**, 920-935 (1996).
- [62] G. P. Lepage and S. J. Brodsky, Phys. Rev. Lett. **43**, 545-549 (1979).
- [63] A. V. Belitsky, X.-d. Ji, and F. Yuan, Phys. Rev. Lett. **91**, 092003 (2003).
- [64] M. Guidal, M. V. Polyakov, A. V. Radyushkin, and M. Vanderhaeghen, Phys. Rev. D **72**, 054013 (2005).
- [65] X.-D. Ji, Phys. Rev. Lett. **78**, 610-613 (1997).
- [66] G. A. Miller, Phys. Rev. Lett. **99**, 112001 (2007) ().
- [67] R. Alkofer and L. von Smekal, Phys. Rept. **353**, 281 (2001).
- [68] C. S. Fischer, J. Phys. G **32**, R253-R291 (2006).
- [69] J. Arrington, K. de Jager, and C. F. Perdrisat, J. Phys. Conf. Ser. **299**, 012002 (2011).
- [70] I. A. *et al.*, ((2009)).
- [71] I. C. C. *et al.*, Few Body Syst. **46**, 1-36 (2009) ().
- [72] A. H. *et al.*, Nucl. Phys. A **755**, 298-302 (2005) ().
- [73] M. G. *et al.* (QCDSF Collaboration), Phys. Rev. D **71**, 034508 (2005) ().
- [74] J. D. A. *et al.*, Eur. Phys. J. A **19**, 9-14 (2004) ().
- [75] R. G. E. *et al.*, PoS LAT2006, 121 (2006) ().
- [76] C. F. Perdrisat, V. Punjabi, and M. Vanderhaeghen, Prog. Part. Nucl. Phys. **59**, 694-764 (2007).